atmosphere

MDPI

Article

Development of an Integrated Lightweight Multi-Rotor UAV Payload for Atmospheric Carbon Dioxide Mole Fraction Measurements

Tonghui Zhao [1,2], Dongxu Yang [1,2,*], Yi Liu [1,2], Zhaonan Cai [1,2], Lu Yao [1,2], Ke Che [1,2], Xiaoyu Ren [1,2], Yongheng Bi [2], You Yi [1,2], Jing Wang [1,2] and Sihong Zhu [1,2]

[1] Carbon Neutrality Research Center (CNRC), Institute of Atmospheric Physics, Chinese Academy of Sciences, Beijing 100029, China; zhaotonghui@mail.iap.ac.cn (T.Z.); liuyi@mail.iap.ac.cn (Y.L.); caizhaonan@mail.iap.ac.cn (Z.C.); yaolu@mail.iap.ac.cn (L.Y.); cheke@mail.iap.ac.cn (K.C.); renxiaoyu@mail.iap.ac.cn (X.R.); yiyou@mail.iap.ac.cn (Y.Y.); jingwang@mail.iap.ac.cn (J.W.); zhusihong@mail.iap.ac.cn (S.Z.)

[2] Key Laboratory of Middle Atmospheric Physics and Global Environment Observation (LAGEO), Institute of Atmospheric Physics, Chinese Academy of Sciences, Beijing 100029, China; byh@mail.iap.ac.cn

* Correspondence: yangdx@mail.iap.ac.cn

Abstract: Records and projections of increasing global average temperature call for improvements of global stocktake inputs, which are vital to achieving targets of intergovernmental agreements on climate change. Unmanned Aerial Vehicle (UAV)-based atmospheric observation of greenhouse gas (GHG) concentrations is an upcoming addition to the top-down measurement methods due to its advantageous spatial-temporal resolutions, greater coverage area and lower costs. Hence, we developed and tested a lightweight UAV payload enclosure integrating a non-dispersive diffusion infrared (NDIR) spectrometer and two electrochemical sensors for measurements of carbon dioxide (CO_2), carbon monoxide (CO) and nitrogen dioxide (NO_2). To achieve higher response times and maintain measurement qualities, we designed a custom air inlet on the rotor-facing side of the enclosure to reduce measurement fluctuations caused by rotor downwash airflow. To validate the payload design, we conducted a controlled test for comparing chambered and chamber-less NDIR spectrometer measurements. From the test we observed a reduction of 0.48 hPa in terms of standard deviation of pressure measurements and minimised downwash-flow-induced anomalous biases (+0.49 ppm and +0.08 hpa for chambered compared to −1.33 ppm and −1.05 hpa for chamber-less). We also conducted an outdoor in-situ measurement test with multiple flights reaching 500 m above ground level (ABGL). The test yielded high resolution results representing vertical distributions of mole fraction concentrations of three types of gases via two types of flight trajectory planning methods. Therefore, we provide an alternative UAV payload integration method for NDIR spectrometer CO_2 measurements that complement existing airborne GHG observation methodologies. Additionally, we also introduced an aerodynamic approach in reducing measurement noises and biases for a low response time sensor configuration.

Keywords: drone-based; carbon dioxide; NDIR; greenhouse gases; rotor downwash; atmospheric observations; emission monitoring

check for updates

Citation: Zhao, T.; Yang, D.; Liu, Y.; Cai, Z.; Yao, L.; Che, K.; Ren, X.; Bi, Y.; Yi, Y.; Wang, J.; et al. Development of an Integrated Lightweight Multi-Rotor UAV Payload for Atmospheric Carbon Dioxide Mole Fraction Measurements. *Atmosphere* **2022**, *13*, 855. https://doi.org/10.3390/atmos13060855

Academic Editors: Ge Han and Miao Zhang

Received: 8 April 2022
Accepted: 22 May 2022
Published: 24 May 2022

Publisher's Note: MDPI stays neutral with regard to jurisdictional claims in published maps and institutional affiliations.

Copyright: © 2022 by the authors. Licensee MDPI, Basel, Switzerland. This article is an open access article distributed under the terms and conditions of the Creative Commons Attribution (CC BY) license (https://creativecommons.org/licenses/by/4.0/).

1. Introduction

Given the results and predictions of the global greenhouse effect and GHG concentrations from the latest studies, it is indisputable that we must continue the improvements of observational capabilities of GHG sources and sinks, both anthropogenic and naturally occurring [1].

Atmospheric CO_2 is one of the most influential GHGs in terms of global warming potential. The unprecedented concentration levels of CO_2 in past decades have been

associated with anthropogenic activities, which contributed to accelerating increases of concentration levels by almost three times (2.39 ± 0.37 ppm yr^{-1} between 2010 and 2019), compared to an average of 0.82 ± 0.29 ppm yr^{-1} during the decade of 1960–1969 [2].

To continue the improvements of global stocktake inputs for achieving the targets of the Paris Agreement, reductions of flux uncertainties require more comprehensive spatial coverages of measurements [3], which demand augmented top-down observation capabilities [4]. Although bottom-up assessment methods are crucial to the accountabilities of global carbon emissions and sinks, posteriori inputs from top-down methods exemplified by atmospheric mole fraction measurements and statistical inversions can improve understandings of carbon fluxes, while bottom-up approaches can reversely validate the results of its counterpart [5] and benefit from the additional constrains provided to the process representations in carbon-cycle models [3].

Atmospheric observations are important to yield top-down measurement results due to their capabilities of retaining large-scale signals and filtering out short-term fluctuations simultaneously [6]. Currently, satellite remote sensing is increasingly available [7] for atmospheric column XCO_2 measurements [8], while regional CO_2 measurements are being conducted by sensors distributed at approximately 100 sites with the supplement of higher towers and manned aircrafts [3]. Being very cost effective, UAVs promise potential contributions by their superior spatial-temporal resolutions and robust weather resistance [9]. To maximise the measurement coverage area for GHGs, UAVs will become formidable additions to the existing network based on ground, aerial and orbital observations. Compared to the current solution of towers and commercial airliners for lower atmospheric measurements, UAVs can provide improved instrument mobility and reduced operational costs. However, there are limitations to applying low-cost UAVs within the field, such as the inability of effectively carrying measurement instruments with large volumes, heavy weights and complex operational procedures. Moreover, although fixed-wing UAVs are generally able to carry heavier payloads, they are unable to measure with low speed.

There have been numerous attempts made to achieve high-precision measurements of GHG concentrations via UAV-based solutions, recent examples of which include a multirotor-drone-mounted active AirCore for methane (CH_4) measurements [10], quantum cascade laser-based CH_4 sensors mounted on a multi-copter drone [11] and a fixed-wing model aircraft [12]. CO2-measuring precedents include a wirelessly connected solar powered UAV sensing system [13], a general airborne-capable payload equipped with SenseAir AB sensor [14] and a Vaisala GMP343 sensor integrated within an unmanned aerial system [9]. The latter examples opted to use a dispersive NDIR spectrometer for CO_2 measurements. This technology was also chosen for the payload described in this study due to its mechanical simplicity and lighter weight, despite the fact that its measurements can be disturbed by rotor downwash airflow. While the benefits of UAV GHG sensing have been proven in previous studies, further payload design challenges such as complex internal component arrangements and maintaining environmental representativeness are yet to be fully addressed. Protecting sensors from downwash airflow generated by propellers is among the foci of this article. Earlier numerical simulation results using fluid dynamic equations for examining interactions between rotor downwash and plumes suggest that onboard gas density measurements vary as a quad-rotor drone flies across the section of a plume [15], indicating perturbed measurements. Another more recent study utilising both computational fluid dynamics and particle imaging velocimetry suggested that there were significant variations in air pressure within the air parcel beneath rotors [16], which was also reflected in the simulation outcome of another similar study [17].

Our objective of developing an enclosed UAV payload for CO_2 measurements is to improve the operational survivability of onboard electronics in less optimal flight conditions. The additional payload enclosure design objective is to redirect vortices and reduce airflow velocities while maintaining low sensor response times. Lastly, payload cost effectiveness is also essential for potential scalability in future operations; therefore, most components of the payload are commercially sourced off-the-shelf products.

The following section introduces instruments integrations and hardware specifications for the payload, while the section emphasis is upon structural and aerodynamic design of the payload enclosure. Section 3 describes the validation tests conducted within a controlled indoor environment, which helped significantly in identifying the anomalous measurement biases caused by rotor downwash airflow. In the same section we also quantitatively present the collected data from several outdoor flights at two different locations in rural Beijing, the obtained results of which serve as proof of design outcome performances for identifying potential rural and urban emission sources. Finally, we summarise the payload development effort and briefly outline some possible future prospects.

2. Materials and Methods

2.1. UAV Platform

DJI Matrice 200 (https://www.dji.com, last access: 23 January 2022) is the sole model of UAV used for the development and testing of the payload. The Matrice 200 is produced by DJI for industrial applications and was discontinued in 2020. With the large-capacity TB55 batteries equipped, the aircraft weighs 4.53 kg, can carry payloads up to 1.61 kg of mass, and has a maximum flight time of 38 min. Its maximum speed for ascent is 5 m/s and the top ceiling for service is 3000 m from sea level, although DJI ordinarily limits the flight height to 500 m above ground level for safety-related reasons. Although there are other manufacturers and drone models that are potentially more suitable for our use in this case, from the perspectives of payload and flight capacities, the DJI Matrice 200 is a good compromise between performance, reliability, flight difficulties and costs.

2.2. Sensors

The primary benefit of the CARBON3060S (OEM version based on Vaisala GMP343 sensor in cooperation with Nanjing ZTweather Technology CO., Ltd. from Nanjing, China. Vaisala GMP343, https://www.vaisala.com, last access: 23 January 2022) NDIR spectrometer for UAV-mounted applications is the absence of moving parts, which reduces the probability of mechanical faults during flights. Accurate ($\pm$1 ppm in 30 s average) in-situ measurements also reduce the time spent between flights. In comparison with AirCore-based techniques, NDIR-based solutions are more portable and easier to deploy, although they are less accurate. CARBON3060S also requires at least 30 min of warm-up time to reach full accuracy ($\pm$0.5% of full accuracy corresponds to a shorter warm-up time of 10 min), resulting in gaps between flights if there is no continuous power supply throughout a mission. Nevertheless, in ideal cases, such continuous power supply is easily available from either a dual-battery drone (able to maintain power output with just one battery while on standby) or a customised port splitter for seamless payload battery swapping. Since the calibrated CARBON3060S measurements had been previously validated against the soundings of tower-mounted Picarro G2301 cavity ring-down spectroscopy analysers with a systematic offset of 0.07 ppm [9], we assumed repeating similar measurement validations to be unnecessary. In addition to factory calibrations according to standard gas at various pressure and temperature levels, the CARBON3060S used in this study went through another calibration procedure in a pressure-controlled environmental chamber prior to tests, and the outcome was validated against synchronous measurements of a PICARRO G2301 cavity ring-down spectroscopic (CRDS) sensor.

For deriving air molar density, we collected meteorological data via a retrofitted radiosonde provided by InterMet, the iMet-4 RSB GPS research radiosonde (https://www.intermetsystems.com, last access: 23 January 2022) measures temperature, relative humidity and pressure at $\pm$0.5 degree Celsius, $\pm$5%, $\pm$2 hPa in terms of uncertainties; 2 s, 5–11 s and 0.5 milliseconds in terms of typical response times, respectively. The radiosonde comes with a separate telemetry module for real-time data transmissions. Since we did not expect circumstances without equipment recoveries, the module was replaced with an interface that facilitates synchronised data collections with other sensors. Meanwhile, the ABGL

height data came from the Matrice 200 flight log file, from which we extracted the inertial measurement unit records and synchronised them with other soundings.

To provide better understandings of emission sources, measurements of gases other than CO_2 are necessary. CO and NO_2 are commonly emitted together with CO_2 in the fossil fuel combustion processes. For example, either separately or simultaneously observed NO_2 can be indicators of spatial [18] and temporal [19] XCO_2 distributions. Thus, for our payload, we used electrochemical sensors NO2-B43F for NO_2 measurements and CO-B4 for CO (https://www.alphasense.com, last access: 23 January 2022), both of which were provided by Alphasense. Their maximum response times are 80 (from zero to 2 ppm) and 30 (from zero to 10 ppm) seconds, respectively. When reaching from 0 to 90% concentration levels of the measured air parcel, the noise levels of soundings of both sensors are ± 2 standard deviations (ppb equivalent). Despite the disadvantage of slow response times, the trace gas soundings yielded potentially usable data, as shown in the results.

2.3. Integrated Payload

To centralise data collection and storage as well as provide power supply, we used a custom designed and manufactured printed circuit board (PCB). The power supply for most electronic components was provided by a 12 V, 2600 mAh lithium-ion battery, which powers the sensors and data collection circuitry for more than two hours in room temperature. As seen in Table 1, the weight of the main battery reduces maximum flight time by more than a minute. Such a reduction is justified by the elimination of extra pre-heating time of CARBON3060S between battery swaps. Meanwhile, the power of radiosonde is supplied by a separate set of CR123A lithium-ion batteries at 3V, weighing 100 g. Ideally, the power should be directly supplied by the UAV for further weight reduction and optimal flight performances; however, to maximise the compatibility between the payload with other drone models, we decided to not dedicate resources to enable direct power supply for a specific drone model. Therefore, we had to temporarily sacrifice design optimality for the sake of payload compatibility and development time.

Table 1. Payload component details with individual information about their weights, power consumptions and influences on maximum flight time of Matrice 200.

	Weight (g)	Power Consumption (w)	Flight Time Reduction (min)
Vaisala CARBON3060S	300	<3.5	3.85
Intermet iMet-4 RSB	62	<0.29	0.79
Alphasense NO2-B43F	20	<0.025	0.25
Alphasense CO-B4	20	<0.025	0.25
Data collection PCB	45	0.48	0.58
18650 Lithium-ion Battery	145	-	1.86
CR123A Lithium-ion Battery	33	-	0.42
Enclosure	323	-	4.13
Other components	149	-	1.91
Total	1097	<4.32	14.04

Designing the payload enclosure involves considerations of component arrangements, operational effectiveness, sensor protections and, most importantly, representativeness of the measured environments. As shown in the sectional view of Figure 1, the internal space of enclosure is sub-divided into two compartments by a panel that creates a measurement chamber and an electronics chamber. Such separation enables different internal environment management strategies between the chambers. With the electronics chamber sealed off with silicate rubber bands for protection from ingress of water and dusts, the sensors in the measurement chamber can also benefit from reduced thermal disturbance since irrelevant heat sources are separated.

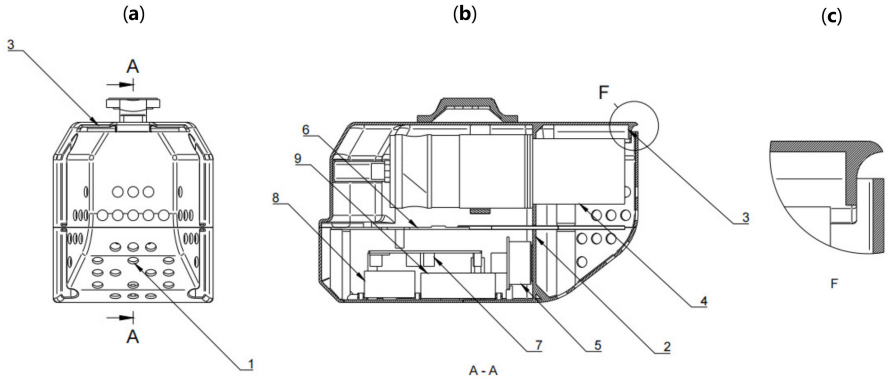


Figure 1. (**a**) Frontal view of the payload enclosure; (**b**) sectional view; (**c**) regional zoomed-in view of air inlet. (1) Ventilation perforations; (2) chamber separator; (3) downwash flow spoiler; (4) CARBON3060S with cap and filter removed; (5) CO-B4 electrochemical sensor; (6) iMet-4 RSB; (7) data collection circuit board; (8) CR123A battery set; (9) 2600 mAh lithium-ion battery set.

The payload enclosure is fabricated via standard fused deposition modelling (FDM) using polylactic acid (PLA) filaments. As the fabrication material is non-isotropic, the structural loads cannot be accurately simulated via finite element analysis (FEA). At 100% infill density during fabrication, the estimated safety factors of the structural design are above three for load cases of maximum ascending and descending speeds. As seen in Figures 1 and 2, the only structural interface between the payload and drone is via the DJI Skyport adapter. The structural design was validated against all possible in-flight structural loads through empirical flight tests. According to the function defining the relationship between take-off weight and flight time, the total mass of payload would result in a 29–37% decrease of maximum flight time for Matrice 200.



Figure 2. Image of the payload mounted on DJI Matrice 200 during a validation test.

Previous studies of measuring gases with sensors onboard UAVs had encountered issues with rotor downwash air flow interfering with the target air parcel [15], leading to measurement inaccuracies. Upon locating the area of vortex occurrences, researchers have concluded that the ideal position for mounting devices sensitive to air flow would be at the geometric centre of quadcopters, either near the plane perpendicular to the rotational axis of propellers [16] or well above it [9]. Our solution is a custom designed measurement chamber structure with protection and ventilation functions. As shown in Figure 3, apart from adding a downwash flow spoiler that reduces air flow velocity at the inlet and redirects flow trajectory, we also minimised the volume of the measurement chamber via a tapered geometry to minimise chamber ventilation time.

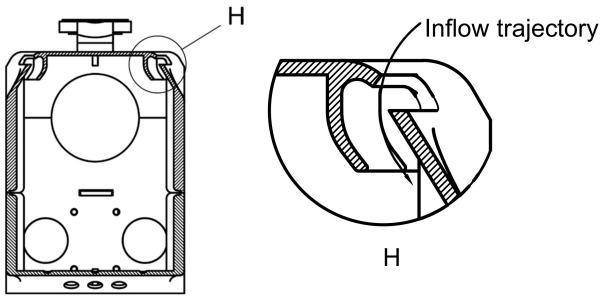


Figure 3. The frontal sectional view of the measurement chamber and zoomed-in view (H) of the downwash flow spoiler responsible for adjustments of flow velocity and direction.

3. Results

3.1. Test for Deriving Rotor Downwash Sensitivity

Despite being compact, lightweight and more portable, thus making dispersive NDIR spectrometry an ideal technology for UAV airborne measurements, rotor downwash airflow can significantly influence its gas measurement accuracies. To determine the exact sensitivity of both CO_2 concentration and air pressure measurements with respect to small UAV rotor induced airflow for CARBON3060S, we designed and conducted a comparative measurement test between two setups which have the same sensor but which are either chambered or chamber-less. Therefore, the test also verified the performance of measurement chamber design on manipulating rotor downwash airflow.

Figure 4 illustrated the respective test setups. To ensure the setups were representative of payload during flight, we needed barometric measurements of static pressure p_s instead of total pressure p_t, hence the barometer air inlet was always perpendicular to the flow direction, following the working principle of a pitot-static tube. The chamber-less test setup was identical in terms of environments and positions with the sole absence of measurement chamber. The selected blower and its distance (40 cm) to the setup were designed to simulate rotor downwash in terms of airflow velocity (approximately 9 m/s given the distance). The flow velocity measurements of both DJI M200's rotor downwash and blower's air outlet were conducted with the same ultrasonic airflow velocity sensor (Vaisala WXT-536 multi-purpose weather station).

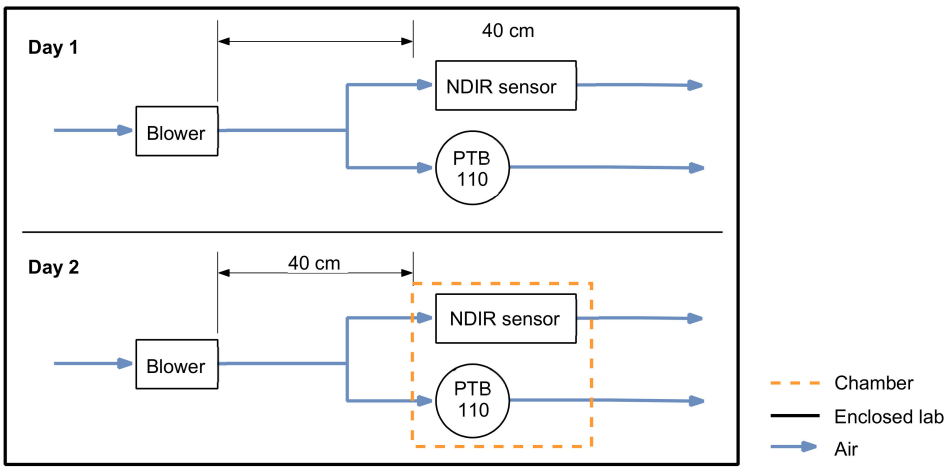


Figure 4. Chambered and chamber-less comparative measurement test setups illustrated with a simplified diagram. The blower is optimally placed and configured to acclerate airflow for producing simulated rotor downwash flow. The indoor environment is relatively enclosed, with no known source or sink of CO_2 and no source of extra airflow. We used a CARBON3060 NDIR sensor and a Vaisala PTB-110 barometer for measuring CO_2 concentration and air pressure.

We performed the test for approximately 48 h, with 24 h each dedicated to the respective setups, which yielded a total of 101 effective test iterations with 46 and 55 iterations for chambered and chamber-less setups. Assuming the measurements sufficiently represent background concentration and pressure when the blower was off, the blower was automatically switched on and off with 10 min intervals for each iteration (Figure 5).

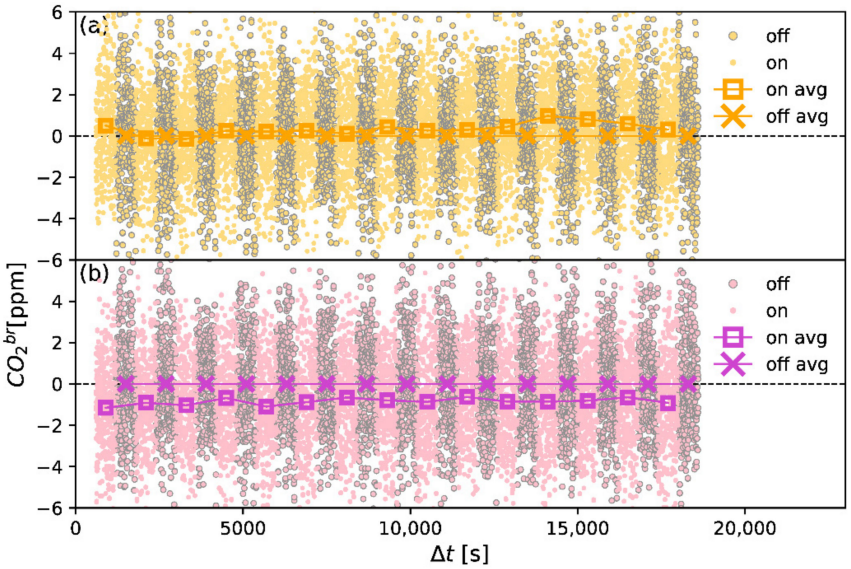


Figure 5. For clarity, we present time series of $CO_2{}^{br}$ (background trend removed with moving average window of 1200 s) of 15 test iterations to exemplify CO_2 concentration anomalous biases relative to the background. Whereas brighter and darker dots represent soundings recorded when the blower was switched on and off, the square and cross markers are averages of each of the segments. Therefore, the differences between averages represent the outcomes of test airflow blowing at chambered (**a**) and chamber-less setups (**b**).

The anomalous biases of CO_2 mole fraction measurements ΔCO_{2_i} are derived according to the following equation,

$$\Delta CO_{2i} = \overline{\boldsymbol{CO_2}_i^{on}} - \overline{\boldsymbol{CO_2}_i^{off}}\ ,\ i\ \in \{1,\ \ldots,\ n\} \tag{1}$$

where i represents each 20 min test iteration and n is the number of effective tests. We simply subtract the mean values of measurements of each blower-off segment $\boldsymbol{CO_2}_i^{off}$ from its adjacent blower-on segment $\boldsymbol{CO_2}_i^{on}$ to derive the anomalous bias of iteration i. Static pressure anomalous bias Δp_{s_i} of iteration i is computed similarly as Equation (2).

$$\Delta p_{s_i} = \overline{\boldsymbol{p}_{\boldsymbol{si}}^{on}} - \overline{\boldsymbol{p}_{\boldsymbol{si}}^{off}}\ ,\ i\ \in \{1,\ \ldots,\ n\} \tag{2}$$

As indicated in Figure 6, anomalous measurement biases for the chamber-less setup far outweigh that of the chambered setup.

To derive the average biases of measurement for chambered ($\Delta CO_2{}^{ch}$) and chamber-less ($\Delta CO_2{}^{cl}$) test setups, we compute the mean of each set of test iterations according to Equations (3) and (4), Average biases for static pressure measurements are derived similarly (Equations (5) and (6)),

$$\Delta CO_2{}^{ch} = \frac{\sum_{i=1}^{m} \Delta CO_{2_i}}{m} \tag{3}$$

$$\Delta CO_2{}^{cl} = \frac{\sum_{i=m+1}^{n} \Delta CO_{2_i}}{n-m} \tag{4}$$

where m is the number of test iterations for chambered setup as it was conducted on the first day, the rest of the iterations (from m + 1 to n) were conducted with chamber-less

setup. Average biases for static pressure measurements (${\Delta p_s}^{ch}$, ${\Delta p_s}^{cl}$) are derived similarly (Equations (5) and (6)).

$$ {\Delta p_s}^{ch} = \frac{\sum_{i=1}^{m} \Delta p_{s_i}}{m} \tag{5} $$

$$ {\Delta p_s}^{cl} = \frac{\sum_{i=m+1}^{n} \Delta p_{s_i}}{n-m} \tag{6} $$

The comparatively anomalous decreases are cases in which the blower turned off for CO_2 and the pressure measurements recorded by the chamber-less setup were 1.33 ppm and 1.05 hpa on average (Figure 6). Meanwhile, the anomalies for chambered setup were less noticeable (increases of 0.49 ppm and 0.08 hpa on average, which we consider to be outcomes of small-scale gas parcel transport and barometer measurement noises), implying that airflow velocity is minimised. Hence, we successfully derived the measurement sensitivities of both soundings to the effect of rotor downwash airflow for our specific case.

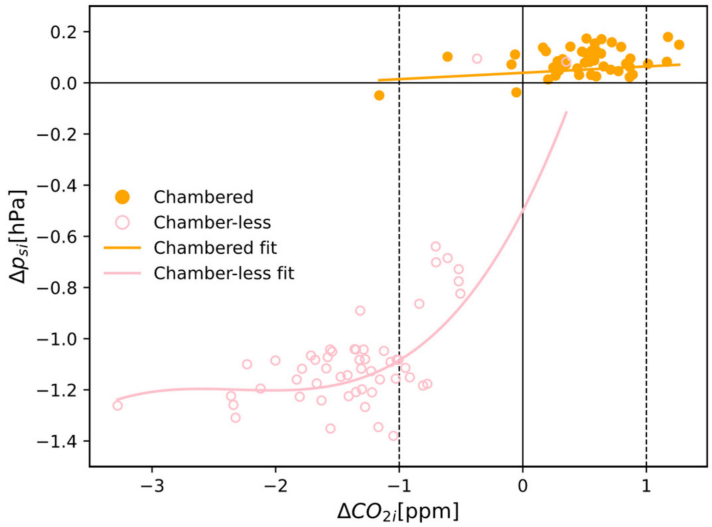


Figure 6. Distribution of mean CO_2 concentration anomalous biases (ΔCO_{2_i}) with respect to mean air pressure anomalous biases (Δp_{s_i}) of individual test iterations for the chambered and chamber-less setups.

We also found the standard deviations of static pressure (σ_{p_s}) and CO_2 (σ_{CO_2}) soundings to be approximately 0.07 hPa, 2.32 ppm and 0.55 hPa, 2.22 ppm for chambered and chamber-less setups, respectively, when the blower was switched on, indicating significantly reduced measurement noises for static pressure when the sensor is chambered. Each CO_2 sounding requires the corresponding air pressure measurement at the same time and space for sensitivity removals. Additionally, given the barometer onboard the payload is mounted so as to ensure its measurement represents static pressure variations within the chamber, it is therefore important that chamber design significantly improves the quality of pressure soundings. Since CO_2 soundings are coupled per 2 s, which means the sensor produces identical soundings for consecutive seconds, we multiply the raw standard deviation by $\sqrt{2}$ to produce an adjusted version of 3.28 ppm and 3.13 ppm for chambered and chamber-less setup test results. Therefore, increased measurement noise levels are more obvious for static pressure instead of CO_2.

The spoiler design in the measurement chamber is hence effective in reducing the influences of rotor downwash airflow upon measurement accuracies and noises. However, the design was unable to fully protect the sensors from vortices, as exhibited in Figure 7.

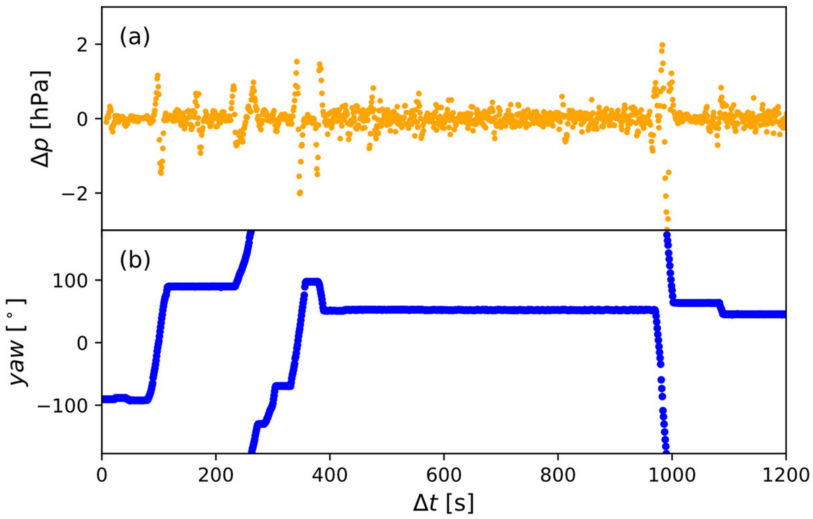


Figure 7. Measurement anomalies of pressure background trend removed with a moving average window size of 16s to capture yaw-related variations during ascent from 0 m to 50 m above ground level of a payload test flight (**a**). As seen from the UAV yaw values (**b**), occurrences of measurement anomalies of pressure coincide with yaw value variations at respective time periods.

Since the enclosure was designed for the aerodynamic loadcase of stable hovering with considerations of other motions or the presence of external flow, we found considerable perterbations from pressure measurements when yawing during a payload test flight. As shown in Figure 7, we were attempting to collect lower tropospheric profile sample data via hovering at several height levels. During hovering for two separate height levels, we inputted control commands to initiate 360-degree yaw cycles which were subsequently identified to be the causes of measurement anomalies. Although CO_2 measurements are relatively less affected, variations of pressure soundings will significantly impact the quality of CO_2 measurement correction in data post-processing, e.g., CO_2 bias correction from pressure shift. According to previous studies of the spatial distributions of multi-copter rotor downwash flow velocities under effects of horizontal airflow [20] and associated vortex characters [16], we consider the aerodynamic cause of measurement anomalies to be due to downwash vortices of rotors propagating into the measurement chamber as the aircraft slowly rotates according to its axis perpendicular to the horizontal plane. It is likely that the vortcies entered through the perforations at the lower section of measurement chamber, which requires further improvements in subsequent designs.

3.2. Lower Boundary Layer Profile Data Collection and Analysis

3.2.1. Test Location

We managed to secure a cylindrical airspace 500 m in diameter and 1 km above ground level height within the Yanqing district of rural Beijing, the mean above-sea-level height of which is approximately 510 m. The ground-level temperature was between 0 to −13 °C because the date of test was the 13 January 2022. As shown in the satellite image of Figure 8, the measurement location is chiefly surrounded by agricultural lands with a mid-sized village on the eastern side. The road seen near the bottom of the image is the main traffic route of the surrounding dwellings and industrial facilities; however, traffic was scarce throughout the test window. The weather of the day was clear with no cloud coverage. There were northwestern winds only during the day time, which was consistent with local prevailing trends. Therefore, we expect a stable near-surface atmospheric condition.



Figure 8. Google Earth satellite image of the test location (bounding box coordinates: 40.48367, 115.84961; 40.48415, 115.86112; 40.47819, 115.86104; 40.47827, 115.84982) and take-off point (40.48141, 115.85544) for all flights. The red cross represents the position where ground level CO_2 sensor was placed. While the yellow pin represents location of take-off and landing, which is approximately 10 m apart from the ground level sensor.

3.2.2. Flight Campaign

As shown in Table 2, we conducted three flights in total during the campaign, with the first flight conducted before sunset and the rest after. To improve understanding of the spatial and temporal attributes of different flight trajectory planning methods, there were two flight methods adopted in this campaign; the ascent and descent of the first two flights were conducted with constant and lowest possible velocity (0.5 m/s), while the ascent of the last flight was based on half-minute hovering at height levels that are 50 m apart. There is nearly no horizontal motion and all three flights reached the above-ground-level height of 500 m. The objective of campaign design is to attempt distinct data collection methods for determining their applicability to different measurements using cases such as initiating atmospheric gas transport models, inversion modelling and conducting real-time emission monitoring.

Table 2. Details of individual flights and their characteristics. Times are in local time zone (UTC+8).

	Flight 1	**Flight 2**	**Flight 3**
Method	**Continuous Ascent**	**Continuous Ascent**	**Level hover Ascent**
Take-off time	16:06:38	19:08:23 [1]	20:09:36
Reached 500 m at	16:20:20	19:20:12	20:17:08
Landing time	16:32:46	19:24:24	20:21:43
Vertical speed	<1 m/s	<1m/s	N/A

[1] Sunset time: 17:11:00.

3.2.3. Synchronous Measurement on the Surface

We placed another integrated payload 10 m away from the take-off point (Figure 8) for comparing background trends of both payloads at ground level. As seen in Figure 9, concentration levels are highly stable before sunset; all spikes before and after flights from payload measurements are caused by test personnel approaching aircraft for powering the system on and off. Spikes seen after sunset were from the same cause, while there was an apparent upward trend in the background CO_2 concentrations which could have been caused by the increase of fossil fuel combustion for heating from the nearby rural

dwellings. Due to the rapidly decreasing temperature after sunset, battery life degraded significantly for flights 2 and 3. To ensure flight safety, we prioritised completing the planned trajectories for the ascents of flight 2 and 3 but descended with full speed. Therefore, only measurements collected during the ascents of all flights are included in atmospheric profile analysis.

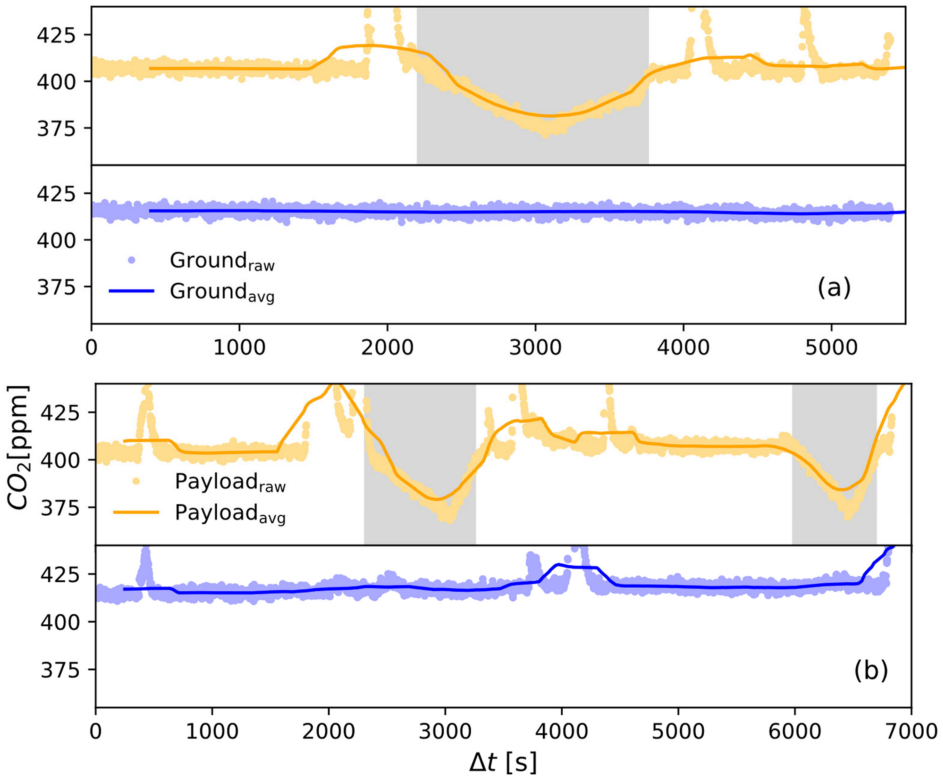


Figure 9. Unprocessed CO_2 measurements from payload and close-proximity ground measurment (Figure 8) for day time (**a**) and night time (**b**). Grey areas separately represent the time intervals of flight 1, 2 and 3. Without any corrections, the difference on average between the measurements of both sensors is approximately 10 ppm throughtout the tests.

3.2.4. Data Processing

Due to the characteristics of the electrochemical sensors for the measurements of CO and NO_2, there is no pre-processing correction applied. For the raw measurements of CO_2 from CARBON3060S, we use a pressure-based polynomial fit correction method before subsequent processing.

In the case of the first flight, there was a deliberate pause at 120m above ground level, which caused an ascent cessation of 80s. The resultant extra measurements are visible on the profile curve for all gas measurements, with an example shown as the smoothened original curve of flight 1 CO measurements in Figure 10. To avoid incorrect representations, we averaged the soundings from 119.4 to 120.4 m with a classification function based on aircraft ABGL height data before running average to produce accurate representations of vertical distributions of individual gas concentrations for flight 1.

As shown in Table 2, the first two flights were conducted with continuous ascents with average air speed of 0.5 m/s. Theoretically, the window sizes of running average computations should be derived from the response times of individual sensors. Nevertheless, such methods would result in either overly noisy results or differed levels of information losses, hence, a uniform 60s window size was found to be a threshold of optimal compromise between measurement representativeness and outcome noise levels. This is exemplified by the comparison between corrected raw data points and its averaged outcome for flight 2 CO_2 measurements in Figure 10.

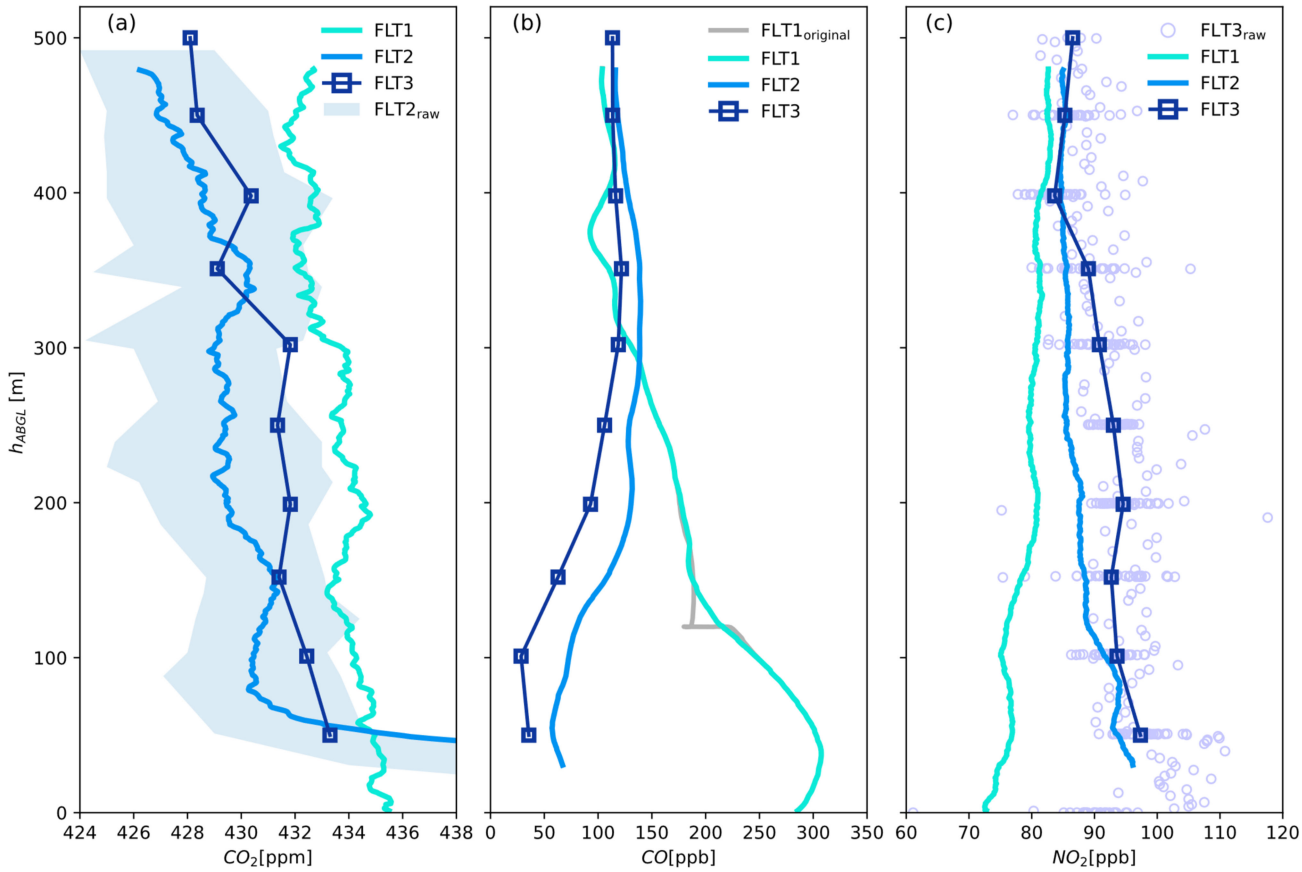


Figure 10. Vertical atmospheric profile of mole fraction density distributions for CO_2 (**a**), CO (**b**) and NO_2 (**c**) during ascent of all three test flights at Yanqing, Beijing. While the moving averages of measurements of the first two flights are plotted with continuous lines, the third flight is exhibited in connected dots (accepted measurements for each height level) due to its distinctive flight trajectory. The three subplots respectively contain information of different data processing methods including simple moving averages of every 60s (flight 2 CO_2), $FLT2_{raw}$ represents area covered by raw measurements, its left and right borders represent maximum deviations from running averages; ascent cessation smoothening (flight 1 CO), $FLT1_{original}$ is the profile without smoothening at the cease flight point; and variance-filtered arithmetic mean for individual height levels (flight 3 NO_2), $FLT3_{raw}$ represents vertical distribution of measurements before filtering and averaging.

Flight 3 was the only test characterised by hovering at each height level; therefore, its post-processing method differs from the continuous flight trajectories. After the pressure-based NDIR CO_2 measurement corrections, measurements of three gases (Figure 10, see flight 3 NO_2 raw measurements for an example) are classified via a function that interprets aircraft vertical velocities (velocities greater than 0.2 or less than −0.03 are regarded as non-hovering datapoints) of individual soundings, so that only soundings registered while hovering are used for outputting accepted measurements (square dots in Figure 10). To derive accepted measurements for each height levels, we filter out soundings that deviate from the level's arithmetic mean by more than three times the level's variance, before the final arithmetic mean is accepted.

3.2.5. Profile Analysis

From the trends of all atmospheric gas measurement plots, there are clear temporal and spatial differences between diurnal and nocturnal profiles. While the temporal distributions of CO_2 and CO follow the trend of higher concentrations near the ground during day time than during night time (approximately 2 ppm and 200 ppb of difference), NO_2 presents the complete opposite (approximately 15 ppb less during day time), signifying

potentially different emission sources, e.g., greater nocturnal activities of vehicles of internal combustion engines on traffic routes south of the take-off point. In terms of spatial distributions, the vertical rate of change of CO_2 is higher than that of the trace gases, with respective values of 8 ppb/m, 0.36 ppb/m and 0.02 ppb/m for the day time flight, and 18 ppb/m, 0.12 ppb/m and 0.02 ppb/m for night time flights. The spike near ground level for flight 2 CO_2 measurement was due to test personnel powering on the drone and performed take-off immediately after, spikes of similar cause can be better seen from Figure 9. Despite CO_2 showing a different tendency, there appear to be a stable boundary layer for the trace gases at roughly 400 m above ground level height. In the meantime, CO_2 measurements present a bifurcation between day time and night time flights from 350 m, with values continuing to decrease for flight 2 and 3 as flight 1 stabilises around 432 ppm. The drop of average CO_2 concentration levels between flights 2 and 3 can be potentially attributable to trends of anthropogenic activities surrounding the flight area, assuming fossil fuel combustion-based heating usage intensifies as nocturnal temperature continues to decrease (flight 2 started 2 h after sunset while flight 3 started 3 h after).

4. Discussion

We designed and manufactured an atmospheric GHG mole fraction measurement UAV payload that integrates a state-of-the-art NDIR spectrometer as well as electrochemical sensors with a customised data collection PCB. The payload enclosure design features at electronics chamber separated from the measurement chamber, which has its own comprehensive airflow management structure designed to relatively isolate internal measurement chamber from multi-copter rotor downwash vortices.

Through simplified fluid dynamic simulations, empirical tests and data analysis, we verified that our custom designed air inlet is effective in stabilising flow within the measurement chamber and maintain its environmental representativeness. In quantitative terms, the anomalous biases from background concentrations on average for the chambered ($\Delta {CO_2}^{ch}$) and chamber-less ($\Delta {CO_2}^{cl}$) test setups are 0.49 ppm and -1.33 ppm, respectively. Hence, the effectiveness of the measurement chamber's aerodynamic design at hover and slow ascent is verified.

Powered by two individual lithium-ion batteries, the payload is able to operate without external power input for at least 3 h, enabling the payload to be mounted on other multi-copter UAV models with a different mounting structure. However, a more optimal solution is to directly supply power from the drone battery, which would increase the maximum flight time by almost 4 min for Matrice 200 if not more for newer models of multi-copters. We look forward to adapting the verified downwash flow spoiler to the next version of payload structural design, which will integrate with other models of multi-copters of different sizes and ascent limitations to achieve greater spatial coverage during missions. We also expect the improvements of the aerodynamic performances of the measurement chamber to accommodate for more flight postures, such as yawing, descent and rolling, to reduce the measurement noises and biases during higher-speed horizontal flights.

After validation flight tests of the payload enclosure design, we conducted a comprehensive flight test for atmospheric profile measurement up to 500 m above-ground-level height on the 13 January 2022 in Yanqing, Beijing. There were two profile measurement techniques attempted, which were embodied by two different flight methods including continuous low speed (0.5 m/s) ascent and intermittent hovering at height levels 50 m apart from each other. Both techniques demonstrated capabilities of accurately representing the atmospheric environment, with the former having a higher spatial resolution (1 m comparing to 50 m). We also observed atmospheric boundary layer effects on the trace gas measurements and the concentration differences before and after sunset.

The democratisation of UAV technologies can improve GHG data availability, especially for the lower atmosphere between 100–1000 m above ground. Proposals included the construction of UAV swarms that simultaneously measure the GHG profiles of the city boundary layer for quantifications of anthropogenic emissions [14]. Mass balance

techniques for measuring the flux density of GHG point sources using UAV-gathered CO_2 and wind data have already been attempted [9], which can benefit from payloads of reduced measurement noises. Alternatively, point source measurements without an onboard anemometer can also be achieved via data fusion techniques that uses meteorological model outputs. In short, the payload development described in this article is a partial representation of the potential application scenarios ideal for UAV atmospheric mole fraction measurements.

Author Contributions: Conceptualization, T.Z. and D.Y.; methodology, T.Z., D.Y., X.R. and K.C.; software, T.Z; validation, T.Z. and D.Y.; formal analysis, T.Z., D.Y. and L.Y.; investigation, T.Z. and D.Y.; resources, Y.L., Z.C. and Y.B. data curation, T.Z., Y.Y., J.W. and S.Z.; writing—original draft preparation, T.Z.; writing—review and editing, T.Z., D.Y. and L.Y.; visualization, T.Z.; supervision, D.Y.; project administration, D.Y.; funding acquisition, D.Y., Y.L. and Z.C. All authors have read and agreed to the published version of the manuscript.

Funding: This work has been supported by the National Key R&D Program of China (Grant No. 2021YFB3901000), the Key Research Program of the Chinese Academy of Sciences (ZDRW-ZS-2019-1).

Data Availability Statement: The data presented in this study are available on request from the corresponding author.

Conflicts of Interest: The authors declare no conflict of interest.

References

1. Arias, P.A.; Bellouin, E.N.; Coppola, R.G.; Jones, G.; Krinner, J.; Marotzke, V.; Naik, M.D.; Palmer, G.-K.; Plattner, J. Technical Summary. In *Climate Change 2021: The Physical Science Basis*; Masson-Delmotte, V., Zhai, P.A., Pirani, S.L.C., Péan, C., Berger, S., Caud, N., Chen, Y., Goldfarb, L., Gomis, M.I., Huang, M., et al., Eds.; Contribution of Working Group I to the Sixth Assessment Report of the Intergovernmental Panel on Climate Change; IPCC: Geneva, Switzerland, 2021.
2. Canadell, J.G.; Monteiro, P.M.S.; Costa, M.H.; da Cunha, L.C.; Cox, P.M.; Eliseev, A.V.; Henson, M.; Ishii, S.; Jaccard, C.K.; Lohila, A.; et al. Global Carbon and other Biogeochemical Cycles and Feedbacks. In *Climate Change 2021: The Physical Science Basis*; Masson-Delmotte, V., Zhai, P., Pirani, A., Connors, S.L., Péan, C., Berger, S., Caud, N., Chen, Y., Goldfarb, L., Gomis, M.H.M.I., Eds.; Contribution of Working Group I to the Sixth Assessment Report of the Intergovernmental Panel on Climate Change; IPCC: Geneva, Switzerland, 2021.
3. GCP. *Science Framework and Implementation. Earth System Science Partnership*; Josep, R.D., Canadell, G., Kathy Hibbard, M.R.O.Y., Eds.; GCP: Canberra, Australia, 2003; p. 69.
4. IPCC. *2006 IPCC Guidelines for National Greenhouse Gas Inventories*; Buendia, L., Ngara, T., Tanabe, K., Eds.; IGES: Kanagawa, Japan, 2006.
5. Liu, J.J.; Bowman, K. A method for independent validation of surface fluxes from atmospheric inversion: Application to CO_2. *Geophys. Res. Lett.* **2016**, *43*, 3502–3508. [CrossRef]
6. Tans, P.P.; Fung, I.Y.; Takahashi, T. Observational Contrains on the Global Atmospheric CO_2 Budget. *Science* **1990**, *247*, 1431–1438. [CrossRef]
7. Yang, D.; Liu, Y.; Boesch, H.; Yao, L.; Di Noia, A.; Cai, Z.; Lu, N.; Lyu, D.; Wang, M.; Wang, J.; et al. A New TanSat XCO2 Global Product towards Climate Studies. *Adv. Atmos. Sci.* **2021**, *38*, 8–11. [CrossRef]
8. Liu, Y.; Wang, J.; Che, K.; Cai, Z.; Yang, D.; Wu, L. Satellite remote sensing of greenhouse gases:Progress and trends. *J. Remote Sens.* **2021**, *25*, 53–64.
9. Reuter, M.; Bovensmann, H.; Buchwitz, M.; Borchardt, J.; Krautwurst, S.; Gerilowski, K.; Lindauer, M.; Kubistin, D.; Burrows, J.P. Development of a small unmanned aircraft system to derive CO_2 emissions of anthropogenic point sources. *Atmos. Meas. Tech.* **2021**, *14*, 153–172. [CrossRef]
10. Andersen, T.; Scheeren, B.; Peters, W.; Chen, H. A UAV-based active AirCore system for measurements of greenhouse gases. *Atmos. Meas. Tech.* **2018**, *11*, 2683–2699. [CrossRef]
11. Tuzson, B.; Graf, M.; Ravelid, J.; Scheidegger, P.; Kupferschmid, A.; Looser, H.; Morales, R.P.; Emmenegger, L. A compact QCL spectrometer for mobile, high-precision methane sensing aboard drones. *Atmos. Meas. Tech.* **2020**, *13*, 4715–4726. [CrossRef]
12. Nathan, B.J.; Golston, L.M.; O'Brien, A.S.; Ross, K.; Harrison, W.A.; Tao, L.; Lary, D.J.; Johnson, D.R.; Covington, A.N.; Clark, N.N.; et al. Near-Field Characterization of Methane Emission Variability from a Compressor Station Using a Model Aircraft. *Environ. Sci. Technol.* **2015**, *49*, 7896–7903. [CrossRef] [PubMed]
13. Malaver, A.; Motta, N.; Corke, P.; Gonzalez, F. Development and integration of a solar powered unmanned aerial vehicle and a wireless sensor network to monitor greenhouse gases. *Sensors* **2015**, *15*, 4072–4096. [CrossRef] [PubMed]
14. Kunz, M.; Lavric, J.V.; Gerbig, C.; Tans, P.; Neff, D.; Hummelgård, C.; Martin, H.; Rödjegård, H.; Wrenger, B.; Heimann, M. COCAP: A carbon dioxide analyser for small unmanned aircraft systems. *Atmos. Meas. Tech.* **2018**, *11*, 1833–1849. [CrossRef]

15. Luo, B.; Meng, Q.-H.; Wang, J.-Y.; Ma, S.-G. Simulate the aerodynamic olfactory effects of gas-sensitive UAVs: A numerical model and its parallel implementation. *Adv. Eng. Softw.* **2016**, *102*, 123–133. [CrossRef]
16. Do, S.; Lee, M.; Kim, J.-S. The Effect of a Flow Field on Chemical Detection Performance of Quadrotor Drone. *Sensors* **2020**, *20*, 3262. [CrossRef] [PubMed]
17. Yang, F.; Xue, X.; Zhang, L.; Sun, Z. Numerical simulation and experimental verification on downwash air flow of six-rotor agricultural unmanned aerial vehicle in hover. *Int. J. Agric. Biol. Eng.* **2017**, *10*, 41–53.
18. Hakkarainen, J.; Ialongo, I.; Tamminen, J. Direct space-based observations of anthropogenic CO_2 emission areas from OCO-2. *Geophys. Res. Lett.* **2016**, *43*, 11400–11406. [CrossRef]
19. Reuter, M.; Buchwitz, M.; Schneising, O.; Krautwurst, S.; O'Dell, C.W.; Richter, A.; Bovensmann, H.; Burrows, J.P. Towards monitoring localized CO_2 emissions from space: Co-located regional CO_2 and NO_2 enhancements observed by the OCO-2 and S5P satellites. *Atmos. Chem. Phys.* **2019**, *19*, 9371–9383. [CrossRef]
20. Lei, Y.; Cheng, M. Aerodynamic Performance of Hex-Rotor UAV Considering the Horizontal Airflow. *Appl. Sci.* **2019**, *9*, 4797. [CrossRef]